Chapter 6

Investigation of anomalous and topological Hall effect in $Ni_{50}Mn_{34}In_{15.2}Al_{0.8}$ magnetic shape memory alloy

In this chapter, we discuss the systematic analysis of the anomalous and topological Hall effect in bulk $Ni_{50}Mn_{34}In_{15.2}Al_{0.8}$ MSMA, which exhibits a stable premartensite phase over a broad temperature range. For a detailed investigation, we conducted temperature- and field-dependent transport measurements over a broad range of temperatures and magnetic fields.

6.1 Introduction

The anomalous Hall effect (AHE) is a fundamental transport phenomenon observed in ferromagnetic materials, characterized by the generation of a transverse voltage in response to a longitudinal electric current, even in the absence of an external magnetic field [1–5]. First reported by Edwin Hall in ferromagnets in 1881 [6], the AHE has since become a key topic in condensed matter physics, owing to its deep connection with the Berry phase [7], topological properties of electronic band structures [8], and spintronic applications [2, 9] , spin-orbitronic devices [10], and Hall sensors [11]. The AHE has thus emerged as a powerful probe for exploring quantum phenomena in magnetic and topological materials, offering insights into their electronic structure and magnetotransport properties. Unlike the normal Hall effect (NHE), which arises from the influence of a magnetic field on the motion of charge carriers, the AHE is result of interplay between magnetism and spin-orbit coupling (SOC) [12–14]. There are two primary mechanisms that explain the AHE in magnetic materials: extrinsic and intrinsic mechanisms. The extrinsic mechanism, which encompasses skew scattering and side-jump processes, is linked to scattering events [15]. In contrast, the intrinsic mechanism arises from the Berry curvature of Bloch bands and remains unaffected by scattering events [16]. The Berry curvature, which acts as a pseudo-magnetic field in momentum space, generates an anomalous velocity in conducting electrons that deflects them in the transverse direction to the electric field, leading to the AHE even without an external magnetic field [17]. Apart from the AHE, another intriguing phenomenon referred to as the topological Hall effect (THE) contributes an additional term to the total Hall resistivity, alongside the NHE and the AHE [18–22]. THE arises from real space Berry curvature originating from non-trivial spin structures such as skyrmions

[18, 23]. THE originates in non-centrosymmetric materials due to Dzyaloshinskii–Moriya interaction (DMI) [24, 25] and in centrosymmetric materials due to the different competing magnetic interactions (magnetic anisotropy, exchange energy, and demagnetization energy) [26, 27]. THE critically depends on the structural phase transition in magnetic shape memory alloys (MSMAs) [28].

Recently, magnetic shape memory alloys (MSMAs) have gained immense interest due to their vast use in technological applications such as magnetically actuated devices [29], energy conversion [30], spintronics [31]. Their growing popularity is driven by their unique functional properties, such as the shape memory effect, giant Hall effect, magnetocaloric effect, exchange bias, magnetoresistance, and Nernst effect. These functional properties of MSMAs are strongly linked to their crystal structures and phase transitions. In general, Ni-Mn-based MSMAs undergo structural phase transition during the cooling from austenite (high symmetry) cubic phase to the martensite phase (low symmetry) at its martensite transition temperature [32–34]. In Ni_2MnGa MSMA, the cubic phase transforms to the martensite phase via an intermediate phase called the premartensite phase (PM-phase) [35–38]. Generally, the Ga-free, Ni-Mn-based MSMA also transforms directly into the martensite phase from the austenite phase while cooling [39]. Recently, some Ga-free MSMAs also undergo the magnetostructural phase transition from austenite (cubic) to martensite (low symmetry phase) via PM-phase during cooling [31, 40, 40, 41]. The magnetotransport study in the PM-phase in these MSMAs is crucial because of exotic phenomena like, skyrmions [28, 31, 42, 43] as the PM-phase facilitates the generation of the skyrmionic texture in the Ni-Mn-In MSMA and is related to the twinning and magnetic anisotropy of the system at phase transition [31]. Generally, the PM-phase lies only in a narrow temperature regime, but a recent study reports that the PM-phase can be stabilized in a wide temperature range using chemical doping [44]. The PM-phase is reported to stabilized in $Ni_{50}Mn_{34}In_{15.2}Al_{0.8}$ MSMA in the wide temperature range by chemical doping [44]. Therefore, the temperature-dependent study of the magnetotransport properties in the PM-phase is important. In the PM-phase, subtle lattice distortions and modulated structures enhance the competition between ferromagnetic exchange and antiferromag-

netic coupling, creating an ideal environment for noncollinear spin configurations.

In the present work, we investigated the AHE and THE in the stable PM-phase of $Ni_{50}Mn_{34}In_{15.2}Al_{0.8}$ MSMA. The origin of AHE is due to the dominant contribution of the Berry phase mechanism. It shows a large THE around the PM transition temperature $\sim$275 K and subsequently decreases with the decrease in temperature. The maximum value of THE is found at higher fields from $\sim$275 K (below 300 K), and this indicates that the larger magnetic field will be required to vanish the topological Hall resistivity at equal or below $\sim$275K, which suggests more stable skyrmion textures. Our findings offer a new direction in functional materials, exhibiting magnetic shape memory and topological effects.

6.2 Methods

A polycrystalline $Ni_{50}Mn_{34}In_{15.2}Al_{0.8}$ MSMA was prepared using arc melting technique with a stoichiometric mixture of high-purity elemental constituents. Melting was performed four times to achieve chemical homogeneity. Afterwards, the resulting ingot was sealed in a quartz ampoule under a vacuum and an argon atmosphere. The sealed quartz tube was then placed in a furnace and annealed at 1073 K for 24 hours to further enhance homogeneity. A small portion of the annealed ingot was cut and ground into a fine powder for characterization. For structural analysis, synchrotron X-ray powder diffraction (SXRPD) measurement was performed using a wavelength of 0.2071 Å at PETRA-III, DESY. Magnetization and transport measurements were carried out using a commercial PPMS (Quantum Design) to study the phase transition and temperature-dependent magnetization behaviour. The temperature-dependent magnetization was recorded under a low magnetic field of 500 Oe. For transport measurements, a small rectangular piece was cut from the bulk sample and polished to minimize measurement errors. Longitudinal resistivity (ρ_{xx}) and transverse (Hall) resistivity (ρ_H) were then measured using a four-probe configuration with indium contacts. Hall resistivity data was first anti-symmetrized to eliminate the longitudinal contribution caused by contact misalignment and then further analyzed to distinguish the different contributions to the Hall resistivity.

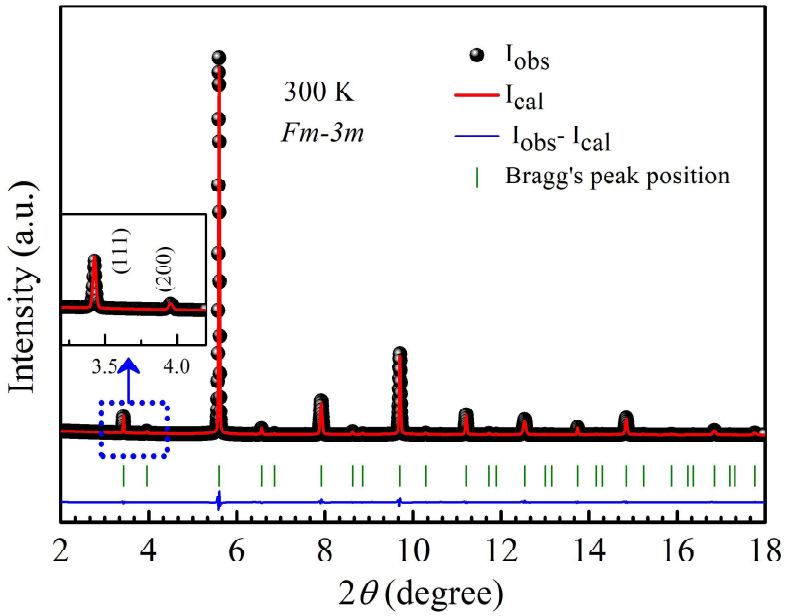

Figure 6.1: Le Bail refinement of synchrotron X-ray powder diffraction (SXRPD) data of $Ni_{50}Mn_{34}In_{15.2}Al_{0.8}$ MSMA at 300 K. The experimental peak profile, calculated peak profile and the difference are shown by black solid circle, red and blue lines, respectively. The green lines represent the Bragg's peak positions. The inset presents a zoomed view of the (111) and (200) superlattice peaks.

6.3 Results and discussion

6.3.1 Structural analysis

The SXRPD data at room temperature was measured to determine the phase purity and crystal structure of the $Ni_{50}Mn_{34}In_{15.2}Al_{0.8}$ MSMA. Le Bail refinement was performed with space group $Fm\bar{3}m$ using FULLPROF software package (Fig. 6.1). The refined lattice parameter is 5.9987 Å. A magnified view of the diffraction pattern between the 3 to 4.5 degrees is displayed in the inset of Fig. 6.1, which confirms the $L2_1$ ordering of the sample.

6.3.2 Magnetization and resistivity

The temperature-dependent magnetization ($M(T)$) was measured at a 500 Oe field, ranging from 385 K to 2 K, using the zero field cooling (ZFC), field cooled cooling (FCC), and field cooled warming (FCW) protocols (Fig. 6.2(a)). The sharp increase in magnetization

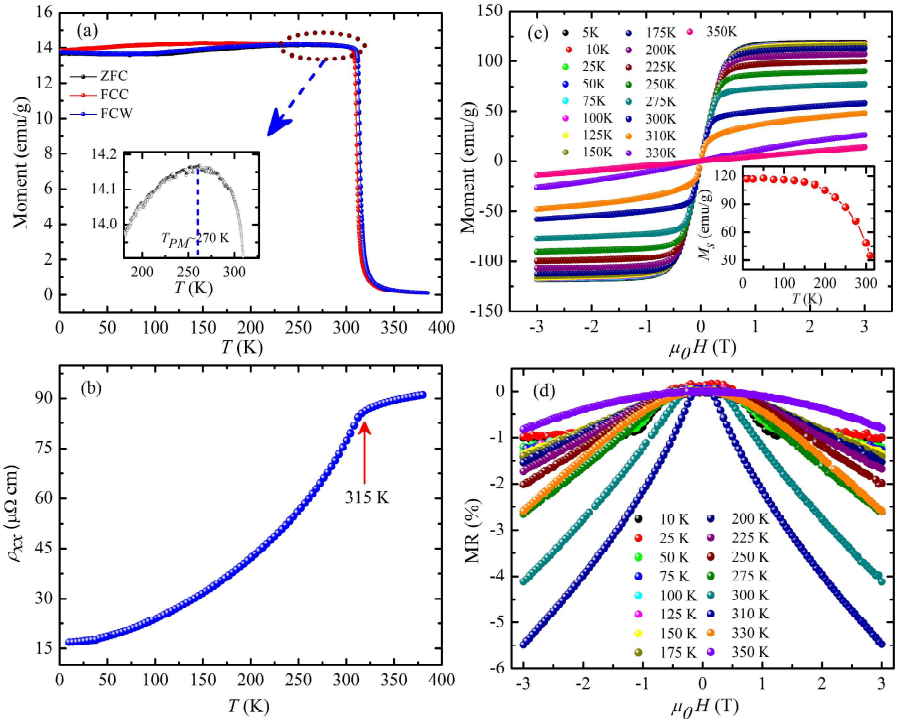

Figure 6.2: (a) Temperature-dependent magnetization plot $M(T)$ of, $Ni_{50}Mn_{34}In_{15.2}Al_{0.8}$ MSMA at 500 Oe. The inset shows the zoomed view of $M(T)$ near the cubic to PM-phase transition temperature. (b) Temperature-dependent longitudinal resistivity (ρ_{xx}) at zero field. (c) Magnetic field-dependent magnetization [$M(H)$] at representative temperatures. Inset shows the saturation magnetization. (d) magnetic field dependent percentage magnetoresistance [MR(%)] at representative temperatures.

around 315 K indicates the second order magnetic transition, where material transforms to the ferromagnetic (FM) state from the paramagnetic. The first-order derivative of the ZFC calculates the $T_C \sim 315$ K. Further cooling, the system undergoes a broad peak below T_C followed by a decrease in magnetization (shown in the inset of Fig. 6.2(a)). The gradually decreasing trend of magnetization with temperature suggests a cubic to PM-phase transition at $\sim$ 275 K [44]. Figure 6.2(b) presents the resistivity as a function of temperature during the heating and cooling. It shows a metallic-like character as resistivity increases with temperature, and no temperature-dependent hysteresis is observed. The sharp change in resistivity observed at $\sim$ 315 K (highlighted with a red arrow) correspond to the T_C, which matches the transition temperature in *M(T)*. The field-dependent magnetization, *M(H)*, is presented in Fig. 6.2(c) for a temperatures range from 350 K to 5 K. At 350 K, the $M(H)$ data reveal paramagnetic behavior. At 330 K, near the onset temperature of the ferromagnetic (FM) transition ($T_C \sim 315$ K), the sample remains predominantly in

the paramagnetic state, with a minor FM component arising due to fluctuations near T_C. Below 330 K, the $M(H)$ curves exhibit a saturating trend at higher magnetic field, indicating the transition into the FM phase. Furthermore, the magnetization reaches higher saturation levels in the PM-phase compared to the austenite phase (inset of Fig. 6.2(c)), owing to the increased magnetocrystalline anisotropy (MCA) in the PM-phase [45]. The percentage change in resistivity under a magnetic field, MR(%), was determined by using the equation:

$$\text{MR (\%)} = \frac{(\rho_H - \rho_0)}{\rho_0} \times 100 \tag{6.1}$$

where $\rho_{xx}(0)$ and $\rho_{xx}(H)$ denote the longitudinal resistivity at zero field and in the magnetic field H, respectively [46–48]. Figure 6.2(d) presents the field dependence of MR(%) in both the austenite and premartensite phases across the temperature range from 350 K to 10 K. The data reveal the presence of negative MR, aligning with observations reported in previous studies on MSMAs [46–48]. Negative MR has also been observed in Ni-Mn-based MSMAs and is explained by the s-d scattering model, where scattering occurs between conduction electrons in s-orbitals and the localized d-spins. [46–48]. The magnetic field aligns the magnetic domains of the d-spins, which reduces s-d scattering and results in negative MR [48]. As the temperature decreases below T_C, the magnitude of negative MR decreases. At ± 3 T, the negative MR is around 0.85% at 350 K (above T_C), 5.5% at 310 K (just below T_C), 2.8% at 275 K (at T_{PM}), and 1.0% at 10 K , as shown in Fig. 6.2(d). The reduced variation in MR at lower temperatures, compared to higher temperatures, is attributed to the reduced s-d scattering [48].

6.3.3 Anomalous Hall analysis

After examining the phase purity and temperature-dependent change in longitudinal resistivity, we performed extensive magnetotransport analysis spanning temperatures from 25 K to 300 K to investigate the AHE in the $Ni_{50}Mn_{34}In_{15.2}Al_{0.8}$ MSMA. Figure 6.3(a) presents ρ_H curves measured in magnetic fields up to 3 T across various temperatures. ρ_H is described by the equation $\rho_H(H) = R_0 H + R_s M$ [5, 49], where R_0 and R_s represent the normal and anomalous Hall coefficients, respectively. H represents the externally ap-

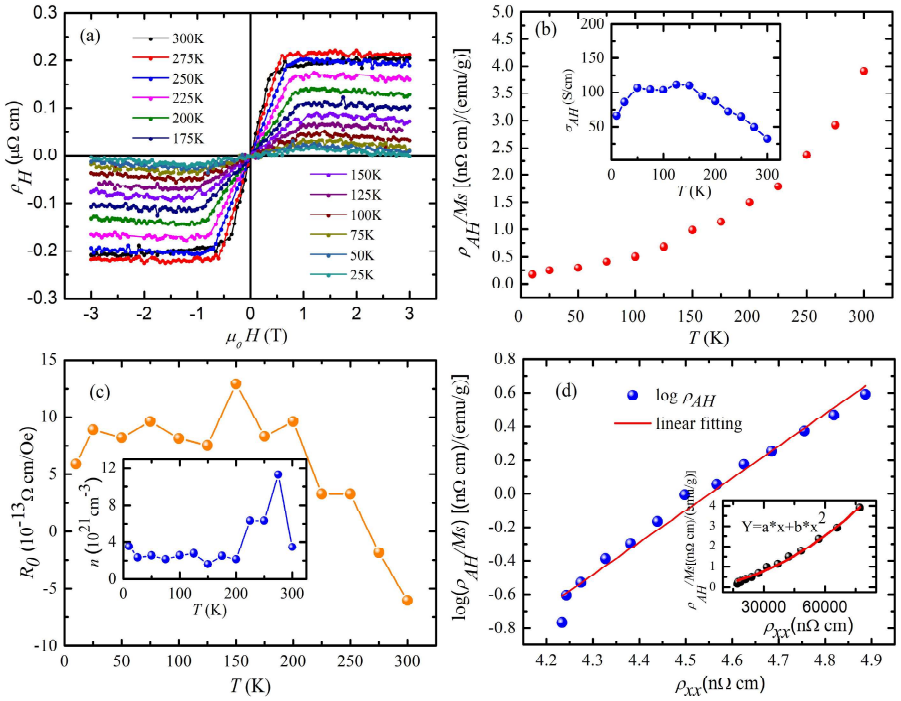

Figure 6.3: (a) Total Hall resistivity (ρ_H) as a function of magnetic filed at the specified temperatures. (b) Anomalous Hall coefficient (ρ_{AH}/M_s).Inset shows the anomalous Hall conductivity. (c) Temperature dependence of the normal Hall coefficient (R_0). Inset displays the variation of carrier concentration n with temperature. (d) The logarithmic plot of ρ_{AH}/M_s vs ρ_{xx} (blue solid circles) with a linear fit is shown by the red line. The inset presents the plot between ρ_{AH}/M_s and ρ_{xx} (black solid circles).

plied magnetic field and M is the magnetization. From Fig. 6.3(a), it can be observed that the initial increase in ρ_H exhibits at lower magnetic fields indicates the presence of the AHE. Furthermore, in the higher field region , ρ_H displays a positive slope following the sign of the normal Hall coefficient. Anomalous Hall resistivity (ρ_{AH}) is determined by extending the high-field Hall data to intersect the ordinate axis at zero field. The intercept represents the Hall resistivity response caused by magnetization of materials at zero field. The variation of ρ_{AH}/M_s with temperature is shown in Fig. 6.3(b). It increases with temperature, reaching its highest value of 4 (nΩ cm $emu^{-1}g$) at the austenite to PM-phase boundary. The variation of anomalous Hall conductivity (AHC) with temperature is shown in the inset of Fig. 6.3(b). The slope of the high-field resistivity curve reveals the normal Hall coefficient (R_0), and the temperature-dependent variation of R_0 are depicted in Fig. 6.3(c). Using the relationship $R_0 = 1/ne$, we determined the density of charge carriers (n), and its variation with temperature is presented in the inset of Fig. 6.3(c). The

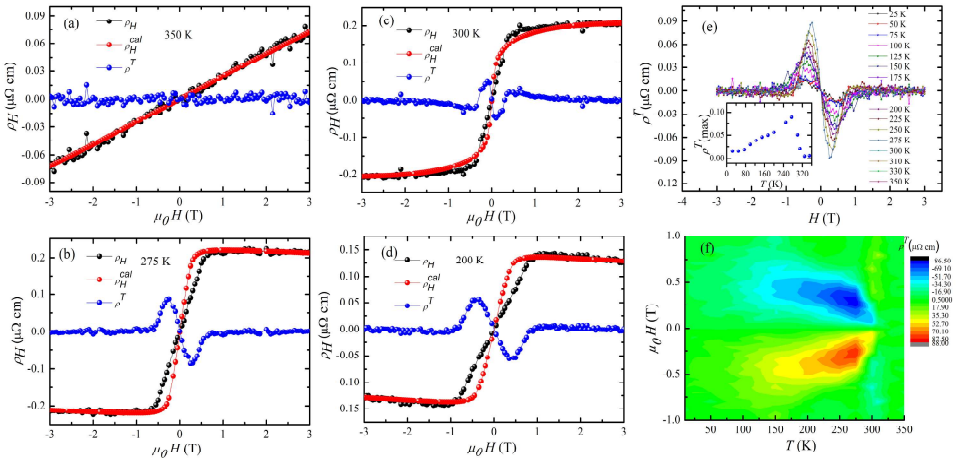

Figure 6.4: The total Hall resistivity (black colour), calculated Hall resistivity (red colour), and extracted topological Hall resistivity (blue colour) curves are shown as a function of magnetic field at (a) 350 K (b) 300 K (c) 275 K (d) 200 K. (e) shows the extracted topological Hall resistivity (ρ^T) at the representative temperatures. Inset depicts the $\rho^T(max)$ as function of temperature. (f) Contour plot of the magnitude of ρ^T.

calculated value for n was approximately 3.5×10^{21} cm^3. The positive R_0 value signifies that holes dominate as the majority of charge carriers in the entire temperature range. To investigate the source of the AHE, anomalous Hall resistivity can be expressed as given equation [50],

$$\rho_{AH} = (a\rho_{xx} + b\rho_{xx}^2)M_s \tag{6.2}$$

$$\rho_{AH}/M_s = a\rho_{xx} + b\rho_{xx}^2 \tag{6.3}$$

Here, a and b represent coefficients associated with extrinsic skew scattering and the combined contributions of intrinsic and extrinsic side jump mechanisms, respectively, while M_s denotes the saturation magnetization. Due to significant variations in saturation magnetization with temperature (inset of Fig. 6.2(c)), it is crucial to consider the magnetization contribution in Eq. 6.2 [51]. We analyzed ρ_{AH}/M_s=R_s vs ρ_{xx} data and plotted on a logarithmic scale. Employing linear regression, we determined the exponent β in accordance with the scaling relation $\rho_{AH} \propto \rho_{xx}^{\beta}$ [52, 53], as shown in Fig. 6.3(d). The parameter β characterizes the relationship between ρ_{AH} and ρ_{xx}. As per established AHE theory, $\beta = 1$ corresponds to AHE originating from the skew scattering mechanism, while $\beta = 2$ is associated with AHE driven by a scattering-independent mechanism [2]. From this anal-

ysis, we found that the exponent $\beta = 1.91$, suggesting that the Berry phase predominantly contributes to the AHE. To identify the various contributions of the underlying mechanisms involved in the AHE, the R_s vs ρ_{xx} data is fitted using Eq. 6.3, as illustrated in the inset of Fig. 6.3(d). After the fitting process, the resulting parameters are $a \sim 1.03 \times 10^{-5}$ (emu/g)$^{-1}$ and $b \sim 0.53$ (Scm^{-1}emu^{-1}g). The intrinsic component of the AHC (σ_H^{int}) can be derived from b by multiplying it with M_s, yielding $\sigma_H^{int} \sim 38$ S/cm at $T \sim 275$ K, corresponds to the austenite to PM-phase transition temperature. Experimentally, AHC (σ_H) was determined using the tensor relation provided below [50].

$$\sigma_H = \frac{\rho_H}{(\rho_{xx}^2 + \rho_H^2)} \tag{6.4}$$

Total AHC was obtained by extrapolating the high-field Hall conductivity data to zero field along the y-axis, yielding a value of ∼49 S/cm at $T \sim 275$ K.This result qualitatively agrees with the calculated σ_H^{int}, indicating that the intrinsic mechanism is the dominant contributor to the total AHC at the austenite and PM-phase boundary.

6.3.4 Topological Hall analysis

In addition to the AHE, we have also evaluated the THE, which has garnered significant attention in recent years, particularly in Heusler alloys [54–56]. The full expression for the total Hall resistivity, including the contribution from THE, is presented below [19, 20, 57–59].

$$\rho_H = \rho_N + \rho_{AH} + \rho^T \tag{6.5}$$

Here, $\rho_N = R_0 H$ represents the NHE, where R_0 is the normal Hall coefficient. ρ^T denotes the topological Hall resistivity. As discussed earlier, the intrinsic contribution to the AHE dominates throughout the entire temperature range below 300 K, covering both the austenite and premartensite phases in $Ni_{50}Mn_{34}In_{15.2}Al_{0.8}$. Consequently, the skew scattering effect on the AHE can be disregarded, allowing us to express R_s as $b\rho_{xx}^2$ in Eq. 6.2. At higher magnetic field, ρ^T disappears as the spin structure transitions from

non-trivial to trivial [57]. Consequently, in this region, Eq. 6.3 can be rearranged as $\rho_H/H = R_0 + b\rho_{xx}^2 M/H$, where the intercept ($R_0$) and slope ($b$) are determined by linearly fitting the plot of ρ_H/H versus $\rho_{xx}^2 M/H$ in the high-field regime [58]. Following the fitting process, the derived values of R_0 and b are utilized to calculate the Hall resistivity as $\rho_H^{cal} = R_0 H + b\rho_{xx}^2 M$ across the entire field range (low and high fields). ρ^T is then obtained by subtracting the calculated Hall resistivity (ρ_H^{cal}) from the experimental Hall resistivity (ρ_H), i.e., $\rho^T = \rho_H - \rho_H^{cal}$. The difference of ρ_H with ρ_H^{cal} at the indicated temperatures is presented in Figs. 6.4(a-d). Figure 6.4(a) displays the field dependence of ρ_H and ρ_H^{cal} at 350 K, which corresponds to the paramagnetic state of the austenite phase. It can be observed that ρ_H and ρ_H^{cal} match perfectly in this phase, leading to the vanishing of THE. As the temperature decreases, the sample transitions to the ferromagnetic (FM) austenite phase near T_C, a small discrepancy between ρ_H and ρ_H^{cal} is observed in the low-field regime, as illustrated in Fig. 6.4(b) at 300 K. This mismatch becomes more pronounced with further cooling, transitioning into the FM PM-phase ($T_{PM} \sim 275$ K). The observed mismatch between ρ_H and ρ_H^{cal} in the austenite and premartensite phases suggests a topological Hall contribution to ρ_H, in conjunction with the normal and anomalous Hall resistivity. [21, 57, 60]. The variation of ρ^T with field is presented in Fig. 6.4(e). ρ^T exhibits a sharp peak, reaching its maximum value at low fields. Temperature-dependence of the maximum value of the topological Hall resistivity (ρ^T(max)) is plotted in the inset of Fig. 6.4(e). The data reveal that ρ^T(max) attains its highest value in the PM-phase. To provide better insight, the contour plot of ρ^T as a function of magnetic field and temperature is shown in Fig. 6.4(f). This map highlights the magnetic field values at which ρ^T(max) reaches its maximum in the austenite and premartensite phases. PM-phase has been proposed to have a strong association with zero-field skyrmion formation in $Ni_{50}Mn_{35.2}In_{14.8}$ MSMA [31], providing a plausible explanation for the occurrence of THE even in the PM-phase. To examine THE in both the austenite and premartensite phases, the temperature dependence of the ρ^T(max) is presented in Fig. 6.4(e). The magnitude of ρ^T(max) is generally considered to be directly proportional to the density of skyrmions and inversely proportional to their size [19]. The elevated value of ρ^T(max) in the PM-phase (around

$T_{PM} \sim 275$ K) might be attributed to the higher nucleation ability of skyrmions at the austenite-to-premartensite phase boundary [19]. It is worthwhile to mention here that a significant increase in the nucleation probability of skyrmions near the magnetic phase transition temperature has been reported in bulk systems [19].

6.4 Conclusion

We investigated AHE and THE in the bulk $Ni_{50}Mn_{34}In_{15.2}Al_{0.8}$ MSMA. The structural and magnetic phase transitions are studied by magnetization and resistivity measurements. We found that the AHE is driven by Berry curvature in momentum space. We also found THE in the system, and it shows the maximum values near the austenite and PM-phase transition. The maximum value of THE in the PM-phase may result from the enhanced nucleation ability of skyrmions at the austenite-to-PM-phase boundary.

References

[1] A. W. Smith, "The Hall effect and the Nernst effect in magnetic alloys," *Phys. Rev.*, vol. 17, no. 1, p. 23, 1921.

[2] N. Nagaosa, J. Sinova, S. Onoda, A. H. MacDonald, and N. P. Ong, "Anomalous Hall effect," *Rev. Mod. Phys.*, vol. 82, no. 2, pp. 1539–1592, 2010.

[3] H. Toyosaki, T. Fukumura, Y. Yamada, K. Nakajima, T. Chikyow, T. Hasegawa, H. Koinuma, and M. Kawasaki, "Anomalous Hall effect governed by electron doping in a room-temperature transparent ferromagnetic semiconductor," *Nat. Mater.*, vol. 3, no. 4, pp. 221–224, 2004.

[4] E. Liu, Y. Sun, N. Kumar, L. Muechler, A. Sun, L. Jiao, S.-Y. Yang, D. Liu, A. Liang, Q. Xu, *et al.*, "Giant anomalous Hall effect in a ferromagnetic kagome-lattice semimetal," *Nat. Phys.*, vol. 14, no. 11, pp. 1125–1131, 2018.

[5] B. Ernst, R. Sahoo, Y. Sun, J. Nayak, L. Muechler, A. K. Nayak, N. Kumar, J. Gayles, A. Markou, G. H. Fecher, *et al.*, "Anomalous Hall effect and the role of Berry curvature in Co_2TiSn Heusler films," *Phys. Rev. B*, vol. 100, no. 5, p. 054445, 2019.

[6] E. H. Hall *et al.*, "On a new action of the magnet on electric currents," *Am. J. Math.*, vol. 2, no. 3, pp. 287–292, 1879.

[7] J. Kübler and C. Felser, "Berry curvature and the anomalous Hall effect in Heusler compounds," *Phys. Rev. B*, vol. 85, no. 1, p. 012405, 2012.

[8] G. K. Shukla, J. Sau, V. Kumar, M. Kumar, and S. Singh, "Band splitting induced Berry flux and intrinsic anomalous Hall conductivity in the NiCoMnGa quaternary Heusler compound," *Phys. Rev. B*, vol. 106, no. 4, p. 045131, 2022.

[9] D. Xiao, M.-C. Chang, and Q. Niu, "Berry phase effects on electronic properties," *Rev. Mod. Phys.*, vol. 82, no. 3, pp. 1959–2007, 2010.

[10] M. Blinov, A. Aryal, S. Pandey, I. Dubenko, S. Talapatra, V. Prudnikov, E. Lähderanta, S. Stadler, V. Buchelnikov, V. Sokolovskiy, *et al.*, "Effects of magnetic and structural phase transitions on the normal and anomalous Hall effects in Ni-Mn-In-B Heusler alloys," *Phys. Rev. B*, vol. 101, no. 9, p. 094423, 2020.

[11] A. Gerber, "Towards Hall effect spintronics," *J. Magn. Magn. Mater.*, vol. 310, no. 2, pp. 2749–2751, 2007.

[12] M.-W. Yoo, J. Tornos, A. Sander, L.-F. Lin, N. Mohanta, A. Peralta, D. Sanchez-Manzano, F. Gallego, D. Haskel, J. Freeland, *et al.*, "Large intrinsic anomalous Hall effect in $SrIrO_3$ induced by magnetic proximity effect," *Nat. Commun.*, vol. 12, no. 1, p. 3283, 2021.

[13] T. Jungwirth, Q. Niu, and A. MacDonald, "Anomalous Hall effect in ferromagnetic semiconductors," *Phys. Rev. Lett.*, vol. 88, no. 20, p. 207208, 2002.

[14] Y. Tian, L. Ye, and X. Jin, "Proper scaling of the anomalous Hall effect," *Phys. Rev. Lett.*, vol. 103, no. 8, p. 087206, 2009.

[15] Q. Zhang, P. Li, Y. Wen, C. Zhao, J. Zhang, A. Manchon, W. Mi, Y. Peng, and X. Zhang, "Anomalous Hall effect in Fe/Au multilayers," *Phys. Rev. B*, vol. 94, no. 2, p. 024428, 2016.

[16] Y. Wang, J. Yan, J. Li, S. Wang, M. Song, J. Song, Z. Li, K. Chen, Y. Qin, L. Ling, *et al.*, "Magnetic anisotropy and topological Hall effect in the trigonal chromium tellurides Cr_5Te_8," *Phys. Rev. B*, vol. 100, no. 2, p. 024434, 2019.

[17] P. K. Rout, P. P. Madduri, S. K. Manna, and A. K. Nayak, "Field-induced topological Hall effect in the noncoplanar triangular antiferromagnetic geometry of Mn_3Sn," *Phys. Rev. B*, vol. 99, no. 9, p. 094430, 2019.

[18] P. Bruno, V. Dugaev, and M. Taillefumier, "Topological Hall effect and Berry phase in magnetic nanostructures," *Phys. Rev. Lett.*, vol. 93, no. 9, p. 096806, 2004.

[19] S. Sen, C. Singh, P. K. Mukharjee, R. Nath, and A. K. Nayak, "Observation of the

topological Hall effect and signature of room-temperature antiskyrmions in Mn-Ni-Ga D_{2d} Heusler magnets," *Phys. Rev. B*, vol. 99, no. 13, p. 134404, 2019.

[20] V. Kumar, N. Kumar, M. Reehuis, J. Gayles, A. Sukhanov, A. Hoser, F. Damay, C. Shekhar, P. Adler, and C. Felser, "Detection of antiskyrmions by topological Hall effect in Heusler compounds," *Phys. Rev. B*, vol. 101, no. 1, p. 014424, 2020.

[21] A. Neubauer, C. Pfleiderer, B. Binz, A. Rosch, R. Ritz, P. Niklowitz, and P. Böni, "Topological Hall effect in the phase of MnSi," *Phys. Rev. Lett.*, vol. 102, no. 18, p. 186602, 2009.

[22] C. Felser and S. Parkin, "Topology, skyrmions, and Heusler compounds," *MRS Bull.*, vol. 47, no. 6, pp. 600–608, 2022.

[23] M. Raju, A. Petrović, A. Yagil, K. Denisov, N. Duong, B. Göbel, E. Şaşıoğlu, O. Auslaender, I. Mertig, I. Rozhansky, *et al.*, "Colossal topological Hall effect at the transition between isolated and lattice-phase interfacial skyrmions," *Nat. Commun.*, vol. 12, no. 1, p. 2758, 2021.

[24] I. Dzyaloshinsky, "A thermodynamic theory of "weak" ferromagnetism of antiferromagnetics," *J. Phys. Chem. Solids.*, vol. 4, no. 4, pp. 241–255, 1958.

[25] T. Moriya, "Anisotropic superexchange interaction and weak ferromagnetism," *Phys. Rev.*, vol. 120, no. 1, p. 91, 1960.

[26] M. Hirschberger, T. Nakajima, S. Gao, L. Peng, A. Kikkawa, T. Kurumaji, M. Kriener, Y. Yamasaki, H. Sagayama, H. Nakao, *et al.*, "Skyrmion phase and competing magnetic orders on a breathing kagomé lattice," *Nat. Commun.*, vol. 10, no. 1, p. 5831, 2019.

[27] R. Takagi, N. Matsuyama, V. Ukleev, L. Yu, J. S. White, S. Francoual, J. R. Mardegan, S. Hayami, H. Saito, K. Kaneko, *et al.*, "Square and rhombic lattices of magnetic skyrmions in a centrosymmetric binary compound," *Nat. Commun.*, vol. 13, no. 1, p. 1472, 2022.

[28] A. K. Singh, G. K. Shukla, and S. Singh, "Intrinsic anomalous Hall conductivity and

real space Berry curvature induced topological Hall effect in Ni_2MnGa magnetic shape memory alloy," *J. Phys. D Appl. Phys.*, vol. 56, no. 4, p. 044004, 2022.

[29] H. E. Karaca, I. Karaman, B. Basaran, Y. Ren, Y. I. Chumlyakov, and H. J. Maier, "Magnetic Field-Induced Phase Transformation in NiMnCoIn Magnetic Shape-Memory Alloys—A New Actuation Mechanism with Large Work Output," *Adv. Funct. Mater.*, vol. 19, no. 7, pp. 983–998, 2009.

[30] J. Liu, T. Gottschall, K. P. Skokov, J. D. Moore, and O. Gutfleisch, "Giant magnetocaloric effect driven by structural transitions," *Nat. Mater*, vol. 11, no. 7, pp. 620–626, 2012.

[31] S. Zuo, F. Liang, Y. Zhang, L. Peng, J. Xiong, Y. Liu, R. Li, T. Zhao, J. Sun, F. Hu, *et al.*, "Zero-field skyrmions generated via premartensitic transition in $Ni_{50}Mn_{35.2}In_{14.8}$ alloy," *Phys. Rev. Mater.*, vol. 2, no. 10, p. 104408, 2018.

[32] X. Moya, L. Mañosa, A. Planes, S. Aksoy, M. Acet, E. F. Wassermann, and T. Krenke, "Effect of external fields on the martensitic transformation in Ni-Mn based Heusler alloys," *Adv. Mater. Res.*, vol. 52, pp. 189–197, 2008.

[33] T. Krenke, M. Acet, E. F. Wassermann, X. Moya, L. Mañosa, and A. Planes, "Martensitic transitions and the nature of ferromagnetism in the austenitic and martensitic states of Ni-Mn-Sn alloys," *Phys. Rev. B*, vol. 72, no. 1, p. 014412, 2005.

[34] M. Krenke and M. ED, "Acet, ef wassermann, x. moya, l. manosa, and a. planes," *Phys. Rev. B*, vol. 73, p. 174413, 2006.

[35] S. Singh, B. Dutta, S. W. D'Souza, M. Zavareh, P. Devi, A. Gibbs, T. Hickel, S. Chadov, C. Felser, and D. Pandey, "Robust Bain distortion in the premartensite phase of a platinum-substituted Ni_2MnGa magnetic shape memory alloy," *Nat. Commun.*, vol. 8, no. 1, p. 1006, 2017.

[36] A. K. Singh, S. Singh, and D. Pandey, "Pair distribution function study of Ni_2MnGa magnetic shape memory alloy: Evidence for the precursor state of the premartensite phase," *Phys. Rev. B*, vol. 104, no. 6, p. 064110, 2021.

[37] V. Chernenko, J. Pons, C. Seguı, and E. Cesari, "Premartensitic phenomena and other phase transformations in Ni-Mn-Ga alloys studied by dynamical mechanical analysis and electron diffraction," *Acta Mater.*, vol. 50, no. 1, pp. 53–60, 2002.

[38] A. Planes, E. Obradó, A. Gonzàlez-Comas, and L. Mañosa, "Premartensitic transition driven by magnetoelastic interaction in bcc ferromagnetic Ni_2MnGa," *Phys. Rev. Lett.*, vol. 79, no. 20, p. 3926, 1997.

[39] X. Moya, L. Mañosa, A. Planes, T. Krenke, M. Acet, and E. F. Wassermann, "Martensitic transition and magnetic properties in Ni–Mn–X alloys," *Mater. Sci. Eng. A*, vol. 438, pp. 911–915, 2006.

[40] Y. Wu, S. Guo, S. Yu, H. Cheng, R. Wang, H. Xiao, L. Xu, R. Xiong, Y. Liu, Z. Xia, *et al.*, "Premartensitic transition and relevant magnetic effects in $Ni_{50}Mn_{34}In_{15.5}Al_{0.5}$ alloy," *Sci. Rep.*, vol. 6, no. 1, p. 26068, 2016.

[41] S. Ma, H. Xuan, C. Zhang, L. Wang, Q. Cao, D. Wang, and Y. Du, "Investigation of the intermediate phase and magnetocaloric properties in high-pressure annealing Ni–Mn–Co–Sn alloy," *Appl. Phys. Lett.*, vol. 97, no. 5, 2010.

[42] S. Singh, J. Bednarcik, S. Barman, C. Felser, and D. Pandey, "Premartensite to martensite transition and its implications for the origin of modulation in Ni_2MnGa ferromagnetic shape-memory alloy," *Phys. Rev. B*, vol. 92, no. 5, p. 054112, 2015.

[43] A. Gonzalez-Comas, E. Obradó, L. Mañosa, A. Planes, V. Chernenko, B. J. Hattink, and A. Labarta, "Premartensitic and martensitic phase transitions in ferromagnetic Ni_2MnGa," *Phys. Rev. B*, vol. 60, no. 10, p. 7085, 1999.

[44] A. K. Singh, S. Singh, B. Dutta, K. Dubey, B. Joseph, R. Rawat, and D. Pandey, "Robust evidence for the stabilization of the premartensite phase in Ni-Mn-In magnetic shape memory alloys by chemical pressure," *Phys. Rev. Mater.*, vol. 5, no. 11, p. 113607, 2021.

[45] J. Enkovaara, A. Ayuela, L. Nordström, and R. M. Nieminen, "Magnetic anisotropy in Ni_2MnGa," *Phys. Rev. B*, vol. 65, no. 13, p. 134422, 2002.

[46] C. Biswas, R. Rawat, and S. Barman, "Large negative magnetoresistance in a ferromagnetic shape memory alloy: $Ni_{2+x}Mn_{1-x}Ga$," *Appl. Phys. Lett.*, vol. 86, no. 20, 2005.

[47] S. Banik, S. Singh, R. Rawat, P. Mukhopadhyay, B. Ahuja, A. Awasthi, S. Barman, and E. Sampathkumaran, "Variation of magnetoresistance in $Ni_{2+x}Mn_{1-x}Ga$ with composition," *J. Appl. Phys.*, vol. 106, no. 10, 2009.

[48] S. Banik, R. Rawat, P. Mukhopadhyay, B. Ahuja, A. Chakrabarti, P. Paulose, S. Singh, A. K. Singh, D. Pandey, and S. Barman, "Magnetoresistance behavior of ferromagnetic shape memory alloy $Ni_{1.75}Mn_{1.25}Ga$," *Phys. Rev. B*, vol. 77, no. 22, p. 224417, 2008.

[49] N. Nagaosa, "Anomalous Hall Effect—A New Perspective," *J. Phys. Soc. Jpn.*, vol. 75, no. 4, pp. 042001–042001, 2006.

[50] K. Otsuka and C. M. Wayman, *Shape memory materials*. Cambridge university press, 1999.

[51] S. J. Murray, M. Marioni, S. Allen, R. O'handley, and T. A. Lograsso, "6% magnetic-field-induced strain by twin-boundary motion in ferromagnetic Ni−Mn−Ga," *Appl. Phys. Lett.*, vol. 77, no. 6, pp. 886–888, 2000.

[52] S. Roy, R. Singha, A. Ghosh, A. Pariari, and P. Mandal, "Anomalous Hall effect in the half-metallic Heusler compound Co_2TiX (X= Si, Ge)," *Phys. Rev. B*, vol. 102, no. 8, p. 085147, 2020.

[53] Q. Wang, Y. Xu, R. Lou, Z. Liu, M. Li, Y. Huang, D. Shen, H. Weng, S. Wang, and H. Lei, "Large intrinsic anomalous Hall effect in half-metallic ferromagnet $Co_3Sn_2S_2$ with magnetic Weyl fermions," *Nat. commun.*, vol. 9, no. 1, pp. 1–8, 2018.

[54] N. Nagaosa and Y. Tokura, "Topological properties and dynamics of magnetic skyrmions," *Nat. Nanotechnol.*, vol. 8, no. 12, pp. 899–911, 2013.

[55] A. Fert, N. Reyren, and V. Cros, "Magnetic skyrmions: advances in physics and potential applications," *Nat. Rev. Mater.*, vol. 2, no. 7, pp. 1–15, 2017.

[56] C. Back, V. Cros, H. Ebert, K. Everschor-Sitte, A. Fert, M. Garst, T. Ma, S. Mankovsky, T. Monchesky, M. Mostovoy, *et al.*, "The 2020 skyrmionics roadmap," *J. Phys. D Appl. Phys.*, vol. 53, no. 36, p. 363001, 2020.

[57] W. Wang, Y. Zhang, G. Xu, L. Peng, B. Ding, Y. Wang, Z. Hou, X. Zhang, X. Li, E. Liu, S. Wang, J. Cai, F. Wang, J. Li, F. Hu, G. Wu, B. Shen, and X.-X. Zhang, "A Centrosymmetric Hexagonal Magnet with Superstable Biskyrmion Magnetic Nanodomains in a Wide Temperature Range of 100–340 K," *Adv. Mater.*, vol. 28, no. 32, pp. 6887–6893, 2016.

[58] J. Gallagher, K. Meng, J. Brangham, H. Wang, B. Esser, D. McComb, and F. Yang, "Robust zero-field skyrmion formation in FeGe epitaxial thin films," *Phys. Rev. Lett.*, vol. 118, no. 2, p. 027201, 2017.

[59] M. Blinov, V. Chernenko, V. Prudnikov, I. Aseguinolaza, J. Barandiaran, E. Lahderanta, and A. Granovsky, "Anomalous Hall effect in $Ni_{47.3}Mn_{30.6}Ga_{22.1}$/Mg O (001) thin films," *Phys. Rev. B*, vol. 102, no. 6, p. 064413, 2020.

[60] D. Amoroso, P. Barone, and S. Picozzi, "Spontaneous skyrmionic lattice from anisotropic symmetric exchange in a Ni-halide monolayer," *Nat. commun.*, vol. 11, no. 1, p. 5784, 2020.